Photoacoustics 31 (2023) 100504

Contents lists available at ScienceDirect

Photoacoustics

journal homepage: www.elsevier.com/locate/pacs

Implantable QR code subcutaneous microchip using photoacoustic and ultrasound microscopy for secure and convenient individual identification and authentication

Nan Wan [a], Pengcheng Zhang [a], Zuheng Liu [a], Zhe Li [c], Wei Niu [d], Xiuye Rui [e], Shibo Wang [a], Myeongsu Seong [f], Pengbo He [a], Siqi Liang [a], Jiasheng Zhou [a], Rui Yang [a,b,*], Sung-Liang Chen [a,g,h,*]

[a] University of Michigan-Shanghai Jiao Tong University Joint Institute, Shanghai Jiao Tong University, Shanghai 200240, China
[b] School of Electronic Information and Electrical Engineering, Shanghai Jiao Tong University, Shanghai 200240, China
[c] Department of Critical Care Medicine, Renji Hospital, School of Medicine, Shanghai Jiao Tong University, Shanghai 200127, China
[d] Department of Nephrology, Huadong Hospital Affiliated, Fudan University, Shanghai 200040, China
[e] Bosch Future Intelligent Driving and Control (Shanghai) R&D Center, Shanghai 200000, China
[f] Department of Mechatronics and Robotics, School of Advanced Technology, Xi'an Jiaotong–Liverpool University, Suzhou 215123, China
[g] Engineering Research Center of Digital Medicine and Clinical Translation, Ministry of Education, Shanghai 200030, China
[h] State Key Laboratory of Advanced Optical Communication Systems and Networks, Shanghai Jiao Tong University, Shanghai 200240 China

ARTICLE INFO

Keywords:
Individual identification and authentication
Implantable devices
Quick response code
Ultrasound microscopy
Acoustic-resolution photoacoustic microscopy

ABSTRACT

Individual identification and authentication techniques are merged into many aspects of human life with various applications, including access control, payment or banking transfer, and healthcare. Yet conventional identification and authentication methods such as passwords, biometrics, tokens, and smart cards suffer from inconvenience and/or insecurity. Here, inspired by quick response (QR) code and implantable microdevices, implantable and minimally-invasive QR code subcutaneous microchips (QRC-SMs) are proposed to be an effective approach to carry useful and private information, thus enabling individual identification and authentication. Two types of QRC-SMs, QRC-SMs with "hole" and "flat" elements and QRC-SMs with "titanium-coated" and "non-coated" elements, are designed and fabricated to store personal information. Corresponding ultrasound microscopy and photoacoustic microscopy are used for imaging the QR code pattern underneath skin, and open-source artificial intelligence algorithm is applied for QR code detection and recognition. *Ex vivo* experiments under tissue and in vivo experiments with QRC-SMs implanted in live mice have been performed, demonstrating successful information retrieval from implanted QRC-SMs. QRC-SMs are hidden subcutaneously and invisible to the eyes. They cannot be forgotten, misplaced or lost, and can always be ready for timely medical identification, access control, and payment or banking transfer. Hence, QRC-SMs provide promising routes towards private, secure, and convenient individual identification and authentication.

1. Introduction

Nowadays, information technology and internet service make people's lives more convenient; meanwhile, the threat of personal information disclosure or theft is also increasing. To ensure personal privacy and information security, user identification and authentication techniques have been ubiquitously deployed in various applications, including access control, payment or banking transfer, transit, individual healthcare, etc.[1–4] Especially, in healthcare and medical emergency situations, timely identification could allow healthcare professionals to quickly retrieve critical medical information such as the blood types, allergies, and anamnesis, which is essential for people that suffer from memory loss and communication disability, such as dementia (e.g., Alzheimer) or loss of consciousness in accidents.[5–7] Generally, identification and authentication information can be carried by three types of media: those based on knowledge such as memorized text or graphic passwords, those based on biometrics such as fingerprints or face recognition, and those based on possession such as physical

* Corresponding authors at: University of Michigan-Shanghai Jiao Tong University Joint Institute, Shanghai Jiao Tong University, Shanghai 200240, China.
E-mail addresses: rui.yang@sjtu.edu.cn (R. Yang), sungliang.chen@sjtu.edu.cn (S.-L. Chen).

https://doi.org/10.1016/j.pacs.2023.100504
Received 9 April 2023; Received in revised form 27 April 2023; Accepted 5 May 2023
Available online 9 May 2023

identifying tokens and smart cards using radio frequency identification (RFID). Research and development towards enhancing privacy and security of user identification and authentication, while maintaining ease of access, have been rapidly emerging.[8].

Passwords are widely used but could be forgotten or stolen, making them inconvenient and insecure for critical information.[9,10] By contrast, biometric identification and authentication by using the biological information that is different for everyone are much more convenient as there is no need to memorize complex passwords, which makes biometrics increasingly popular.[9–11] However, biometrics still suffer from privacy disclosure and insecurity because the biometric credentials employed in the authentication system are part of user privacy, and are difficult to be hidden or kept secret in practical environment.[12,13] For example, the face information and even iris information can be recorded in high resolution pictures, the fingerprints are left on objects after touching, and the voice can also be recorded or generated. The leaked biological information could be maliciously applied to faking/replay attacks at the biometric identification and authentication system and could lead to heavy loss.[12,13].

Besides biometrics, RFID plays an important role in the identification and authentication as well.[14–16] RFID-based contactless smart cards, which are particularly versatile, are applied to a number of security-sensitive applications, such as electronic passports, physical access control, and contactless credit cards for payment systems.[17,18] In particular, for healthcare systems, an RFID bracelet or necklace worn by a patient could mitigate the risk of misidentification and improve patient management.[19] However, RFID bracelets or necklaces can be misplaced, forgotten, or lost. In 2004, the first implantable RFID microchip, which was known as VeriChip and allowed patient identification, was approved by the U.S. Food and Drug Administration.[20] While both non-implanted and implanted RFIDs are useful for various identification and authentication purposes, RFID implants as "prosthetic biometrics" are more convenient as they are automatically carried with people when implanted.[21,22] Nevertheless, non-implanted and implanted RFID chips still suffer from security threats, because RFID tags can be accessed wirelessly and instantaneously without individual awareness or consent.[16,23] Specifically, spoofing attacks can be performed by scanning RFID tags or by eavesdropping on data exchanged between RFID tags and readers, whether the RFID tags are implanted or not.[21].

Quick response (QR) code, a type of two-dimensional (2D) barcode that can carry various information, now becomes more and more frequently used in daily life.[24,25] Normally, QR code encodes information with the arrangement of "black" and "white" square elements, which correspond to "0" and "1", respectively, and can thus be easily recognized by computing systems using the decoding rules. Then the information will be further processed automatically and efficiently, including information storage, comparison with the information in the database, linking to the webpages, etc. Accordingly, QR code has been widely used in a variety of applications: not only in inventory tracking and product marketing, but also in individual identification and authentication, such as QR-code-based access control systems and QR code printed on cards as proof of identity.[24,26–28] In particular, for healthcare purposes, QR code identity tags (e.g., QR code identity bracelets or necklaces) have been employed for outpatient identification and medical emergency in some medical facilities.[29].

In this work, inspired by implantable chips and QR code technology, we demonstrate an individual identification and authentication method, named QR code subcutaneous microchip (QRC-SM), towards enhanced privacy and security while maintaining ease of access. Here the QRC-SM under skin can carry useful and private information, and imaging techniques are used for retrieving the information. We explore ultrasound-related imaging techniques including ultrasound microscopy (USM) and acoustic-resolution photoacoustic microscopy (AR-PAM), which is one kind of implementation of photoacoustic imaging, to provide sufficient penetration depth and spatial resolution for imaging QRC-SMs. Corresponding to the two imaging modalities, two types of QRC-SMs are designed and fabricated, respectively. As ultrasound is sensitive to the depth of reflective surfaces, we design and fabricate QRC-SMs using "hole" and "flat" elements (with different depth) on a silicon (Si) chip to stand for the "black" and "white" elements in the conventional QR code image, respectively, and the difference in the time of receiving the reflected ultrasound signal (i.e., time of flight) is used for reconstruction of the original QR code image by USM. As photoacoustic imaging is sensitive to optical absorption, we also design and fabricate QRC-SMs using "titanium (Ti)-coated" (strong optical absorption) and "non-coated" (weak optical absorption) elements to stand for the "black" and "white" elements in the conventional QR code image, respectively, and the different photoacoustic signal strength is used to for reconstruction of the original QR code image by AR-PAM. Furthermore, we have performed both *ex vivo* imaging of the QRC-SM under chicken breast tissue and in vivo imaging of the QRC-SM implanted into a nude mouse, and demonstrated reliable retrieval of the QR code pattern and the encoded information. In the experiments, we showcase four application scenarios that involve individual identification and authentication, including individual healthcare, company access control, payment or banking transfer, and a link to a website for showing more identity information. The patterns on QRC-SMs that are hidden subcutaneously ensure the privacy of personal information, in contrast to biometrics and identity objects (stickers, bracelets, necklaces, etc.) that are exposed. In addition, QRC-SMs almost cannot be stolen, lost, misplaced or forgotten like physical identifying tokens, thus providing both security and convenience. Another advantage of ultrasound-related imaging for QRC-SMs is the requirement of coupling media contact, which avoids the eavesdropping and spoofing attacks, and in this regard, QRC-SMs are superior to RFID implants accessed by non-contact readout through wireless transmission. Therefore, these QRC-SMs may open interesting opportunities for widespread implantable microchips with functionalities including private, secure, and convenient individual identification and authentication.

2. Results

2.1. Principle and design of QRC-SMs

We illustrate the working principles of the QRC-SMs imaged by USM and AR-PAM in Fig. 1. Fig. 1A shows a QRC-SM with "hole" and "flat" elements under skin, and the difference in the time of flight of back-scattered ultrasound from "hole" and "flat" elements is employed for imaging. Fig. 1B shows a QRC-SM with "Ti-coated" and "non-coated" elements under skin, and the difference in the strength of photoacoustic signals from "Ti-coated" and "non-coated" elements is used for imaging. Specifically, the design of QRC-SMs consists of three steps and is tightly correlated with the chosen biomedical imaging methods.

The first step is the consideration of suitable imaging techniques that can retrieve the QR code patterns under skin. Pure optical imaging techniques such as optical coherence tomography, multiphoton microscopy, and confocal microscopy have limited penetration depth of ~1 mm due to the strong optical scattering of tissue, and are less preferred for noninvasive imaging of objects under skin [30,31]. To noninvasively image objects or patterns under skin, ultrasound-related imaging techniques are good candidates because of the high penetration depth of ultrasound in tissue. Thus, two imaging modalities that involve ultrasound, ultrasound imaging and photoacoustic imaging, are selected. Besides, designing the QR code patterns as small as possible under skin is important as it can minimize the influence on tissue and provide convenience for implanting. Therefore, we choose the method of microscopy to image the small QR code patterns under skin. Combining the need of ultrasound-related imaging techniques and the need of microscopy, in this work, we select USM and AR-PAM to image QR code patterns under skin. For AR-PAM, pulsed laser at near-infrared wavelength of 1064 nm, within the biological window, is chosen for

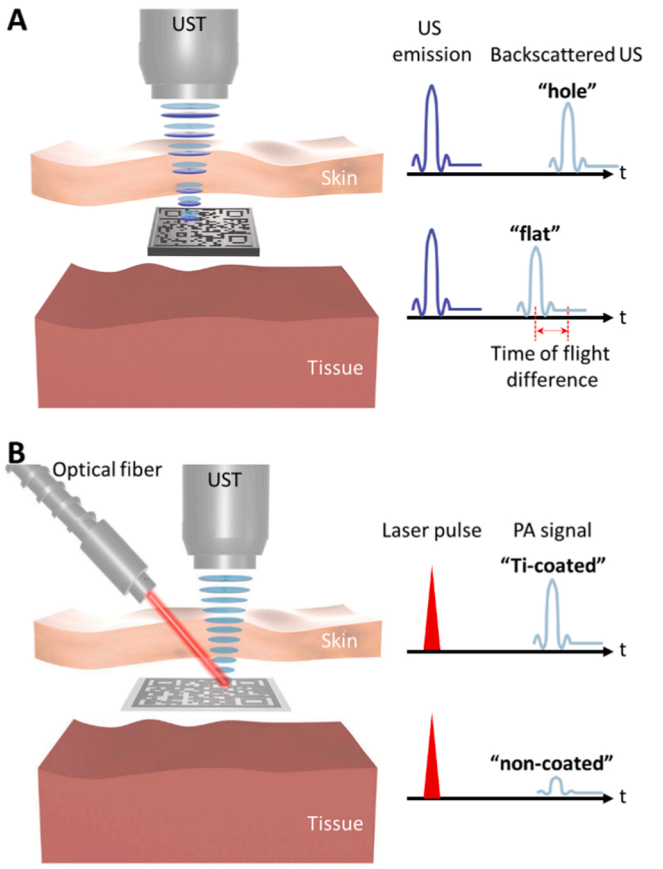

Fig. 1. Working principles of QRC-SM. A) QRC-SM with "hole" and "flat" elements coupled with USM for identification and authentication. B) QRC-SM with "Ti-coated" and "non-coated" elements coupled with AR-PAM for identification and authentication. Note that QRC-SMs are hidden subcutaneously and invisible to the eyes. UST, ultrasound transducer; US, ultrasound; PA, photoacoustic.

photoacoustic excitation to ensure sufficient penetration.[32,33].

The second step is determining the materials and structures of the QRC-SMs based on the selected imaging modalities. To create QRC-SMs allowing ultrasound imaging, we select Si chips that can offer hard reflective surfaces. We then design the QRC-SMs with "hole" and "flat" elements on the Si chips, and when the ultrasound transducer is scanned across the "hole" and "flat" elements, the time difference for receiving the reflected signal can stand for the "black" and "white" elements in the conventional QR code image (Fig. 2 A), respectively, forming a depth-encoded image. The three-dimensional (3D) schematics of the QRC-SM with "hole" and "flat" square elements are shown in Fig. 2B (top view) and 2 C (tilted view), which resemble a labyrinth. The "hole" patterns are defined lithographically and etched down into the Si chip, forming the "hole" and "flat" structure. In addition, Si is also biocompatible and can ensure safety when implanted into the human body [34]. To create QRC-SMs allowing photoacoustic imaging, which is sensitive to optical absorption, we lithographically define the regions to coat 100 nm Ti on a Si dioxide (SiO_2) substrate. Ti is chosen because it has much stronger optical absorption at the wavelength of 1064 nm than SiO_2 (1.084×10^6 cm^{-1} versus 115.54 cm^{-1}) and thus can generate a stronger photoacoustic signal [35,36]. The contrast in the photoacoustic signal amplitude can be used to form the photoacoustic image in 2D maximum amplitude projection (MAP) to reflect the original QR code pattern. Corresponding to the same conventional QR code image with "black" and "white" elements (Fig. 2 A), the 3D schematics of the QRC-SM with "Ti-coated" elements and "non-coated" elements (SiO_2) are shown in Figs. 2E and 2 F. It is also important that Ti and SiO_2 are biocompatible [34], and can ensure the safety for the human body. A layer of polydimethylsiloxane (PDMS) is coated on the surface of the chips to protect the chips for long-term operation and ensure even better biocompatibility [34,37].

The third step is determining the size of each square element in QRC-SMs, so that every element can be resolved by the microscopy system we used. For QRC-SMs with "hole" and "flat" elements, the size of each element is designed based on the resolution of the USM system. In our USM (see Fig. S1A in the Supporting Information), a flat ultrasound transducer with 50-MHz central frequency and a 77% nominal bandwidth is used. An acoustic lens is attached on the transducer to provide an NA of 0.44 and a focal length of 6.7 mm. Accordingly, the lateral resolution of the USM system is calibrated as 52 μm (Fig. 2I) by imaging the sharp edge of a blade. Therefore, we design the length of each "hole" and "flat" element as 100 μm, which is adequate for resolving adjacent elements in the ultrasound image and can enable reliable QR code recognition. In addition, the depth resolving capability of the USM system is calibrated as around or smaller than 10 μm (Fig. 2H) by using the time at the peak of the envelope of ultrasound A-line signals (ultrasound pressure versus time). The depth can be then calculated accordingly with the known sound speed. When setting different reference depths (ground truth) with 10 μm interval of a reflector by using a motorized stage, USM can discriminate the different depths (Fig. 2H), although the measured depth by USM is always a bit smaller than the reference depth, which might be because the motorized stage does not precisely move to the designated position. Therefore, we design the depth of each "hole" element as 30 μm, which is adequate for discriminating the "hole" and "flat" elements. As shown by the example in Fig. 2D, each "hole" or "flat" element has a length of 100 μm and a depth (for "hole" element) or a height (for "flat" element) of 30 μm. Similarly, for QRC-SMs with "Ti-coated" and "non-coated" elements, the size of each element is designed based on the resolution of the AR-PAM system. In the AR-PAM system (see Fig. S1B in the Supporting Information), a pulsed laser that emits light at wavelength of 1064 nm is used. Upon laser irradiation, strong photoacoustic signals are generated from the "Ti-coated" elements, while those elements without Ti coating show much lower signals because SiO_2 has very low optical absorption. Then the photoacoustic signals are collected by the same 50-MHz ultrasound transducer (with the acoustic lens attached) used in the USM system. The lateral resolution of the AR-PAM system is then calibrated as 65 μm (Fig. 2 J), which is slightly larger than the USM system. To leave enough safety margin for resolving neighboring elements, we design the length of each "Ti-coated" or "non-coated" element as 150 μm. As shown by the example in Fig. 2 G, each single "Ti-coated" and "non-coated" square element has a length of 150 μm and a thickness of 100 nm. Note that considering the lateral resolution, a smaller feature size may be designed, yet the QR code pattern becomes more obscure, which impairs its successful recognition.

2.2. *Applications, fabrication and characterization of QRC-SMs*

To demonstrate the applications of our QRC-SMs for individual identification and authentication, we encode four representative messages in four QR code patterns, each representing a type of critical information for a certain identification and authentication scenario. The first representative QR code pattern encodes the message of "Eric Li: Type B, Asthma" (Pattern No. 1, see Fig. S2A in the Supporting Information), which describes a virtual person's name, blood type and anamnesis. This showcases that the QRC-SM is useful for efficient and timely medical identification in individual healthcare and emergency scenarios. Healthcare professionals can quickly retrieve critical medical information from both outpatients and emergency patients. The second representative QR code pattern encodes the message of "Eric Li: CHASE, 123456789″ (Pattern No. 2, see Fig. S2B in the Supporting Information), which describes virtual bank account information including user name, bank name and account number. This demonstrates that the QRC-SM

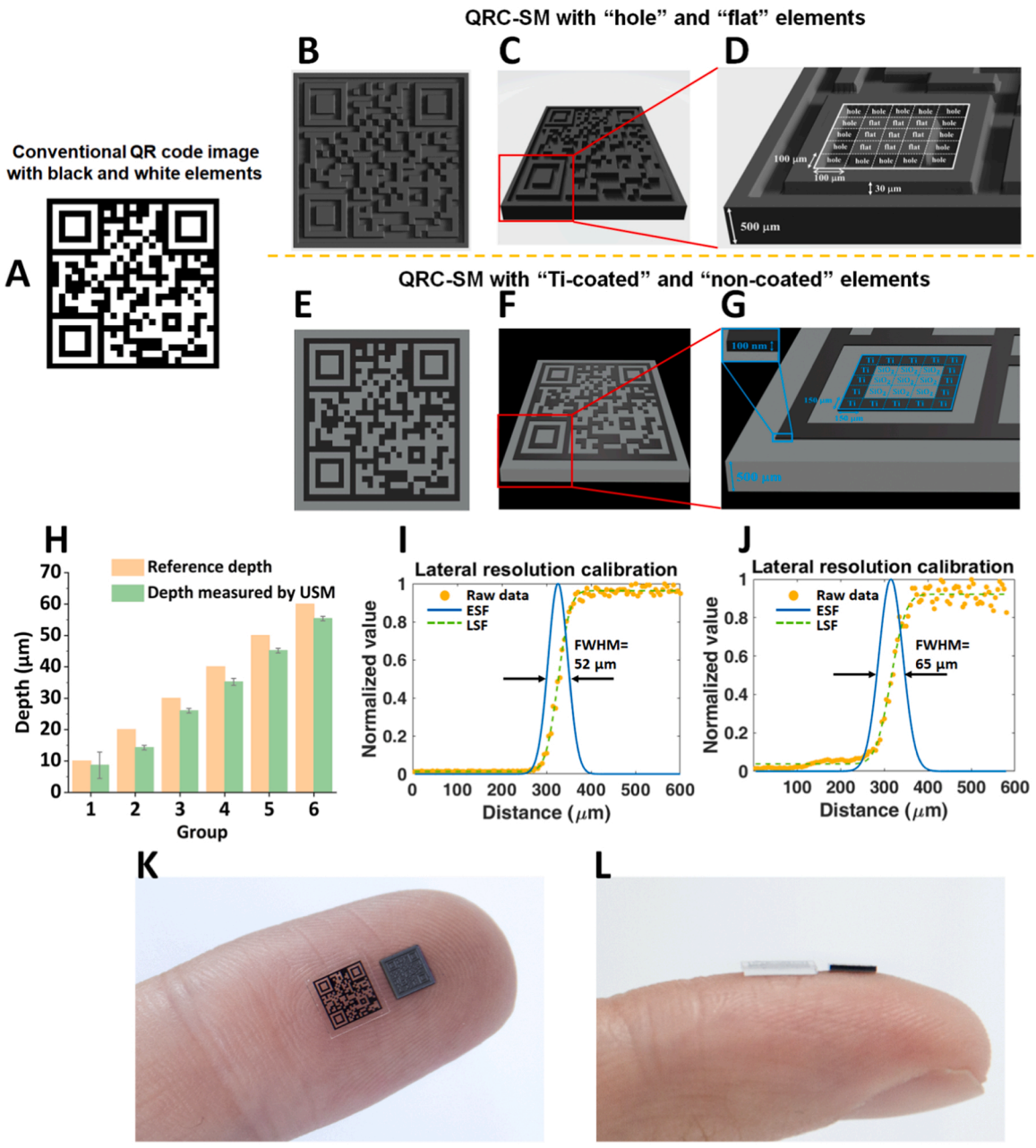

Fig. 2. Design, fabrication, and initial characterization of QRC-SM. A) Conventional QR code image with "black" and "white" elements. B) to D) QRC-SM with "hole" or "flat" elements for USM: (B) 3D schematic (top view), (C) 3D schematic (tilted view), and (D) Zoomed-in view from the red box in (C) showing the feature size of the QRC-SM and the "hole" or "flat" elements. E) to G) QRC-SM with "Ti-coated" and "non-coated" elements for AR-PAM: (E) 3D schematic (top view), (F) 3D schematic (tilted view), and (G) Zoomed-in view from the red box in (F) showing the feature size of the QRC-SM and the "Ti-coated" or "non-coated" elements. H) Measured depth resolving capability of USM. I) Resolution calibration of USM. J) Resolution calibration of AR-PAM. K) Front view of the two types of QRC-SMs laid side by side on a finger, with the one with "Ti-coated" and "non-coated" elements on the left, and the one with "hole" and "flat" elements on the right. L) Side view of the two types of QRC-SMs on a finger.

can be employed for identification and authentication in the process of payment or banking transfer so that individual account security and asset security can be ensured. The third representative QR code pattern encodes the message of "Eric Li: Engineer of Google, 035″ (Pattern No. 3, see Fig. S2C in the Supporting Information), which describes a virtual employee named Eric Li, the employer, the position and the employee number. This demonstrates that the QRC-SM can be applied to access control for institutions with high security level such as some companies and government agencies. Not only physical access control, which refers to entering a room or building, but also access control for online service can be realized by using such an identification and authentication technique. The fourth representative QR code pattern encodes the message of "https://www.ji.sjtu.edu.cn" (Pattern No. 4, see Fig. S2D in the Supporting Information), a link to the website of the University of Michigan-Shanghai Jiao Tong University Joint Institute. We set it as an example to demonstrate that the QRC-SM can be used for linking to a personal website, so that more identity or other information can be retrieved for identification and authentication, despite the finite capacity of the QR code itself.

As shown in Fig. S2 (Supporting Information), all the four QR code patterns consist of 27 × 27 square elements, and each element is either "black" or "white". Based on these four patterns, we make the photomask to fabricate QRC-SMs using photolithography. The detailed fabrication process is shown in Fig. S3 (Supporting Information). As we

design each "hole" and "flat" element with a length of 100 μm, the whole size of the QRC-SM for ultrasound imaging is about 3 mm × 3 mm (Fig. 2 K). After fabrication, the four QRC-SMs with "hole" and "flat" elements are imaged by optical microscopy (see Figs. S4A–S4D in the Supporting Information). Similarly, as we design each "Ti-coated" and "non-coated" element with the length of 150 μm, the total size of the QRC-SM for photoacoustic imaging is about 4.3 mm × 4.3 mm (Fig. 2 K and see Figs. S4E–S4H in the Supporting Information). The thickness of the Si chip with "hole" and "flat" elements and the SiO_2 chip with "Ti-coated" and "non-coated" elements are both about 500 μm (Fig. 2 L). Both types of chips have a 5-μm-thick layer of PDMS film for packaging and protection.

2.3. Imaging QRC-SMs with "hole" and "flat" elements using USM

We first use a step profiler (LSM 800 Zeiss) to scan the fabricated QRC-SMs to verify the exact depth of the etched "holes" (Fig. 3A), which is about 30 μm. Then, to evaluate the imaging performance of the QRC-SMs with "hole" and "flat" elements, we image four QRC-SMs using USM without any tissue on top, which correspond to the four representative applications mentioned above. During imaging, we scan the ultrasound transducer across the QRC-SMs with a scanning step size of 20 μm in both X and Y directions and record the time of flight between sending and receiving the ultrasound signal. After imaging, open-source artificial intelligence algorithm published by WeChat Computer Vision Team is applied to QR code detection and recognition [38]. For convenience, we term this algorithm as "CVQR" in the following description. Readers are also encouraged to use WeChat application or other QR code scanning applications to scan the images and verify the personal information retrieval.

We show the imaging results for QRC-SMs that depict pattern No. 3 as an example. The depth-encoded image is shown in Fig. 3B. Setting the depth-encoded image as an input, the personal information "Eric Li: Engineer of Google, 035″ can be retrieved using CVQR algorithm. A representative B-mode image (cross-sectional image along the lateral and depth directions), corresponding to the blue dashed line in Fig. 3B, is shown in Fig. 3C, where the "hole" and "flat" elements with different depths are clearly imaged. Similarly, for bare QRC-SMs that depict No. 1, No. 2 and No. 4 patterns, the depth-encoded images are shown in Figs. S5A–S5C (Supporting Information).

To demonstrate the ability of depth penetration of our USM system, we image a QRC-SM with "hole" and "flat" elements (also pattern No. 3 as an example) covered by a 2.3-mm-thick layer of chicken breast tissue, under which the QRC-SM is hidden and invisible to eyes. Chicken breast tissue has been frequently used in various ultrasound or photoacoustic imaging studies to test the penetration depth [39–41]. In addition, practically, the ultrasound scanning direction X (or Y) may not be parallel to the boundary of the QR code pattern, and, therefore, we image QRC-SMs covered by chicken breast tissue with a set angle of ~45° between the scanning direction X (or Y) and the boundary of the QR code pattern. With a scanning step size of 20 μm, we obtain the depth-encoded image (Fig. 3D) and the personal information "Eric Li: Engineer of Google, 035″ using the CVQR algorithm.

To demonstrate the whole process of implanting the QRC-SM with "hole" and "flat" elements and retrieving the personal information with USM and CVQR algorithm, we have further performed in vivo experiments (Fig. 4) also using the QRC-SM depicting pattern No. 3 as an example. Specifically, an 8-weeks-old adult nude mouse is anesthetized, and then a small incision in its skin is made with the size just enough for implanting the QRC-SM (Fig. S5D). Then, a QRC-SM (No. 3 pattern) with "hole" and "flat" elements is implanted under its skin (Fig. 4 A and 4B). After implantation, the QR code pattern is covered by mouse skin and is thus totally hidden and cannot be seen (Fig. 4 C). Later, USM is applied for imaging with a scanning step size of 20 μm. The depth-encoded image obtained from the in vivo measurement is shown in Fig. 4D, and the personal information of "Eric Li: Engineer of Google, 035″ is retrieved by the CVQR algorithm. Fig. 4E shows the workflow of the CVQR algorithm for retrieving the information from the depth-encoded image of a QRC-SM, and Fig. 4 F– 4I are the corresponding step-by-step outputs. Specifically, using a depth-encoded image (Fig. 4 F) as the

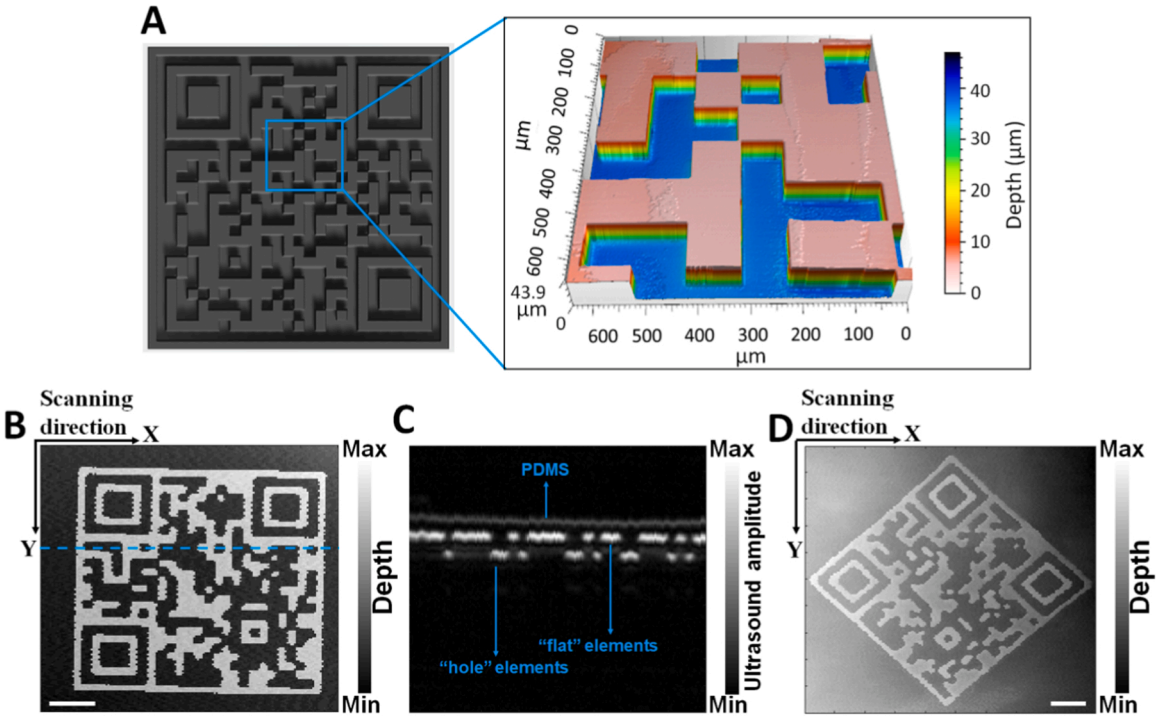

Fig. 3. *Ex vivo* imaging of a QRC-SM with "hole" and "flat" elements. A) Illustration of the 3D structure of a QRC-SM with "hole" and "flat" elements (Pattern No. 3), and the color map of the depth profile measured by a step profiler. B) USM image of a bare QRC-SM (Pattern No. 3). C) B-mode image corresponding to the dashed blue line in (B). D) USM image of a QRC-SM (Pattern No. 3) covered by a 2.3-mm-thick layer of chicken breast tissue. Scale bars, 500 μm.

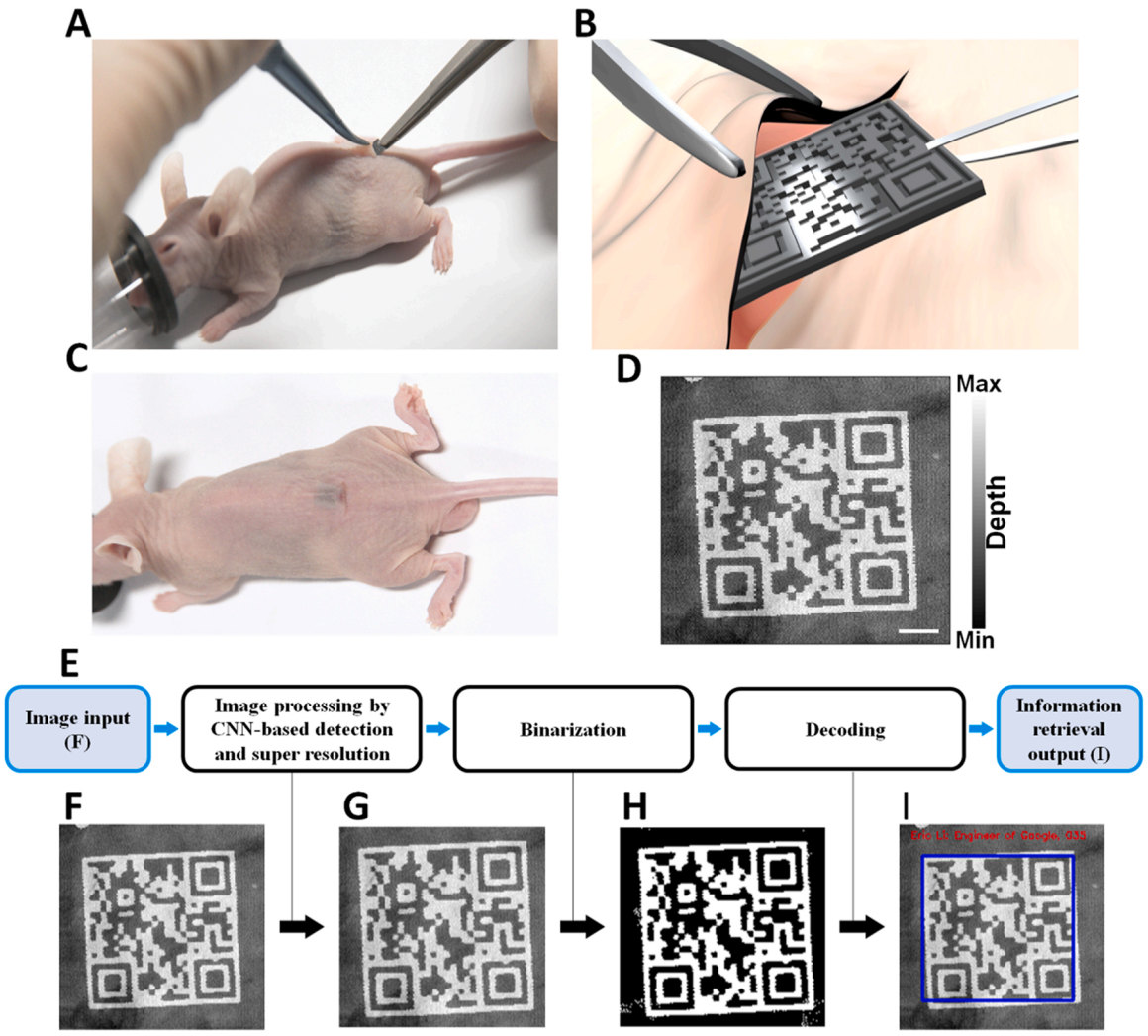

Fig. 4. *In vivo* experiments of a QRC-SM with "hole" and "flat" elements. A) Photograph showing the process of implanting a QRC-SM into a nude mouse. B) 3D schematic of implanting a QRC-SM underneath mouse skin. C) A nude mouse with an implanted QRC-SM such that the QR code patterns are hidden underneath the mouse skin. D) USM image of the QRC-SM implanted into the nude mouse. E) Workflow of the CVQR algorithm for retrieving the information from depth-encoded image of a QRC-SM. F) Depth-encoded image as input. G) Output after CNN-based detection and super resolution. H) Output after binarization. I) Final output. Scale bar, 500 μm.

input, the CVQR algorithm first processes the data using a convolutional neural network (CNN) for detection and super resolution (Fig. 4 G), and then binarization is performed (Fig. 4H). Lastly, the binarized result is decoded, and the CVQR outputs a final result (Fig. 4I). Note that the final output includes the retrieved information and a rectangle drawn on the initial input (Fig. 4 F), which is used to locate the position of the QR code in the image.

2.4. Imaging QRC-SMs with "Ti-coated" and "non-coated" elements using AR-PAM

We also perform AR-PAM measurements on four types of QRC-SMs

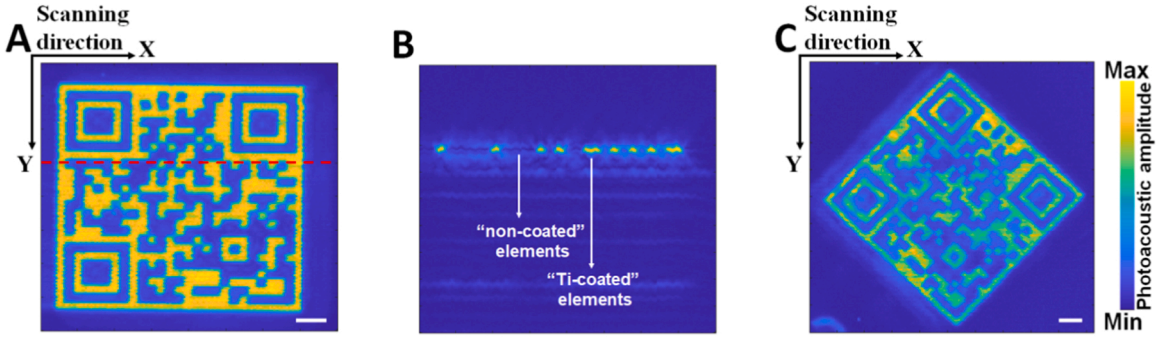

Fig. 5. *Ex vivo* imaging of a QRC-SM with "Ti-coated" and "non-coated" elements. A) AR-PAM image of a bare QRC-SM (Pattern No. 1). B) B-mode image corresponding to the dashed red line in (A). C) AR-PAM image of a QRC-SM (Pattern No. 1) covered by a 2.3-mm-thick layer of chicken breast tissue. Scale bars, 500 μm.

with "Ti-coated" and "non-coated" elements to demonstrate the capability of identification and authentication. We show the MAP image of a bare QRC-SM with No. 1 pattern as an example (Fig. 5A). Setting the MAP image as an input, the personal information "Eric Li: Type B, Asthma" is retrieved using the CVQR algorithm. During imaging, the scanning step size is 30 μm for both X and Y directions. A representative B-mode image, corresponding to the red dashed line in Fig. 5A, is shown in Fig. 5B, where "Ti-coated" and "non-coated" elements with different photoacoustic amplitudes are clearly imaged. Similarly, for QRC-SMs that depict No. 2, No. 3 and No. 4 patterns, the MAP images are shown in Figs. S6A–S6C (Supporting Information).

To demonstrate the ability of depth penetration of our AR-PAM system, we also image the QRC-SM (also pattern No. 1 as an example) covered by a 2.3-mm-thick layer of chicken breast tissue with a set angle of ~45° between the scanning direction and the boundary of the QR code pattern. With a scanning step size of 30 μm, the MAP image is shown in Fig. 5C, and the personal information "Eric Li: Type B, Asthma" can be retrieved by the CVQR algorithm.

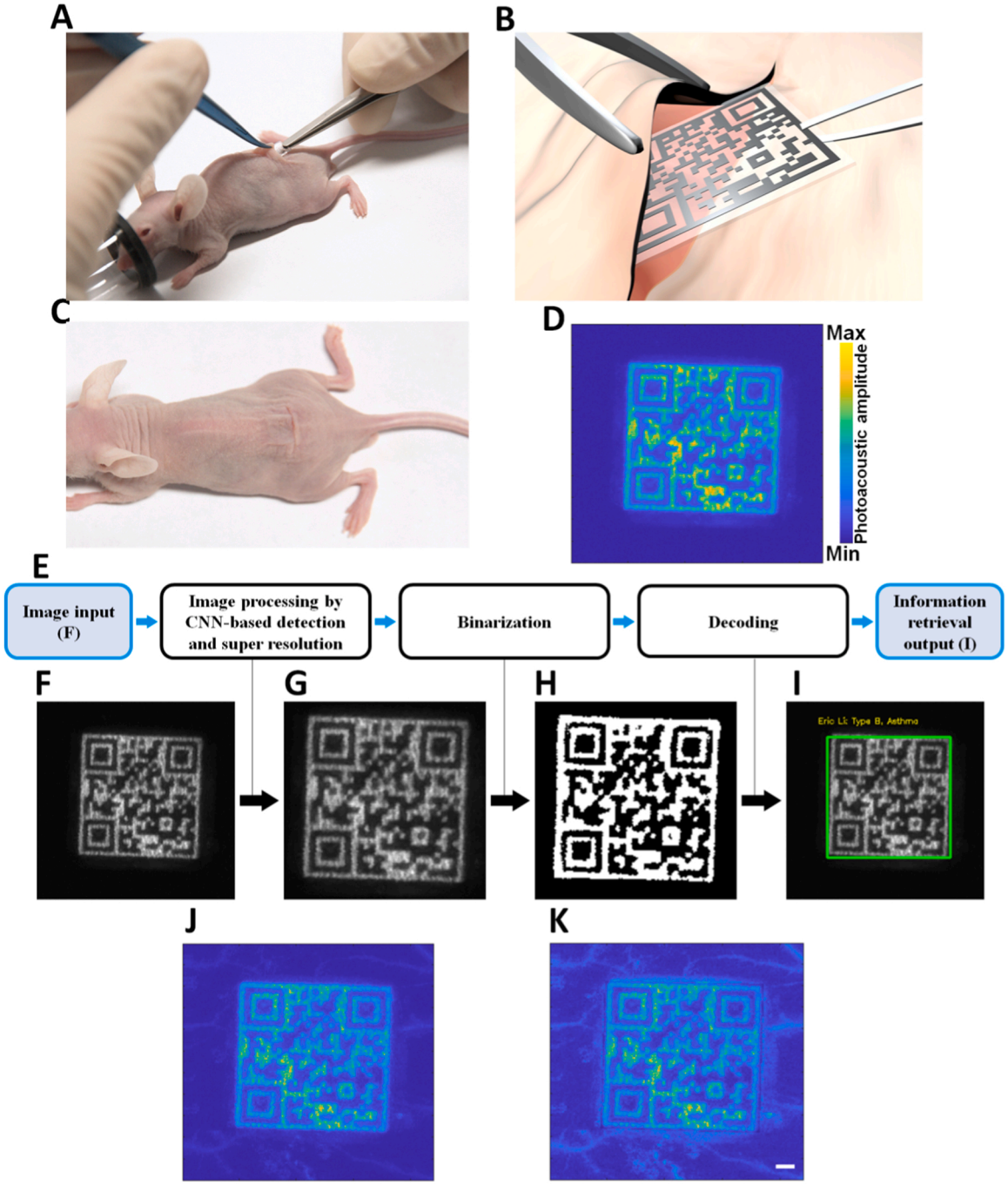

Fig. 6. *In vivo* experiments of a QRC-SM with "Ti-coated" and "non-coated" elements. A) Photograph showing the process of implanting a QRC-SM into a nude mouse. B) 3D schematic of implanting a QRC-SM underneath mouse skin. C) A nude mouse with an implanted QRC-SM such that the QR code pattern is hidden under the mouse skin. D) AR-PAM image of the QRC-SM implanted into the nude mouse. E) Workflow of the CVQR algorithm for retrieving the information from MAP image of a QRC-SM. F) MAP image as input. G) Output after CNN-based detection and super resolution. H) Output after binarization. I) Final output. J) AR-PAM image of the same QRC-SM implanted in the nude mouse imaged using laser wavelength at 670 nm. K) AR-PAM image with vessels enhanced based on (J). Scale bar for (D, J and K), 500 μm.

We also perform in vivo experiments by imaging the QRC-SM with "Ti-coated" and "non-coated" elements using AR-PAM. The process of implanting the QRC-SM (No. 1 pattern) into an 8-weeks-old adult nude mouse is shown in Fig. 6 A– 6 C. Similarly, a small incision in its skin is made, with the size just enough for implanting the QRC-SM (see Fig. S6D in the Supporting Information). Then AR-PAM is employed for imaging with laser wavelength of 1064 nm and a scanning step size of 30 μm. The MAP image (Fig. 6D) can be clearly observed, and the personal information "Eric Li: Type B, Asthma" is successfully retrieved by the CVQR algorithm. Similarly, Fig. 6E shows the workflow of the CVQR algorithm, and Fig. 6 F– 6I are corresponding step-by-step outputs. If we adjust the wavelength to 670 nm, besides the QR code pattern, we can also image the vessels under the skin (Fig. 6 J), which results from the optical absorption of hemoglobin. Interestingly, vessels in the MAP image do not affect the QR code recognition. To present the vessels more clearly, based on Fig. 6 J, the amplitude of the area outside the QR code pattern is intentionally enhanced by two times, as shown in Fig. 6 K. This demonstrates the robustness of our imaging technique and CVQR algorithm for retrieving the correct encoded information in the complex environment in a living body.

As for the scanning time, in vivo imaging of QRC-SMs with "hole" and "flat" elements by USM takes 3.5 min, with a step size of 20 μm. When we increase the step size to 40 μm (see Fig. S7A in the Supporting Information), information retrieval can still be realized, and the scanning time is decreased to about 1.1 min. On the other hand, in vivo imaging of QRC-SMs with "Ti-coated" and "non-coated" elements by AR-PAM takes 7.7 min, with the step size of 30 μm. When we increase the step size to 60 μm (see Fig. S7B in the Supporting Information),

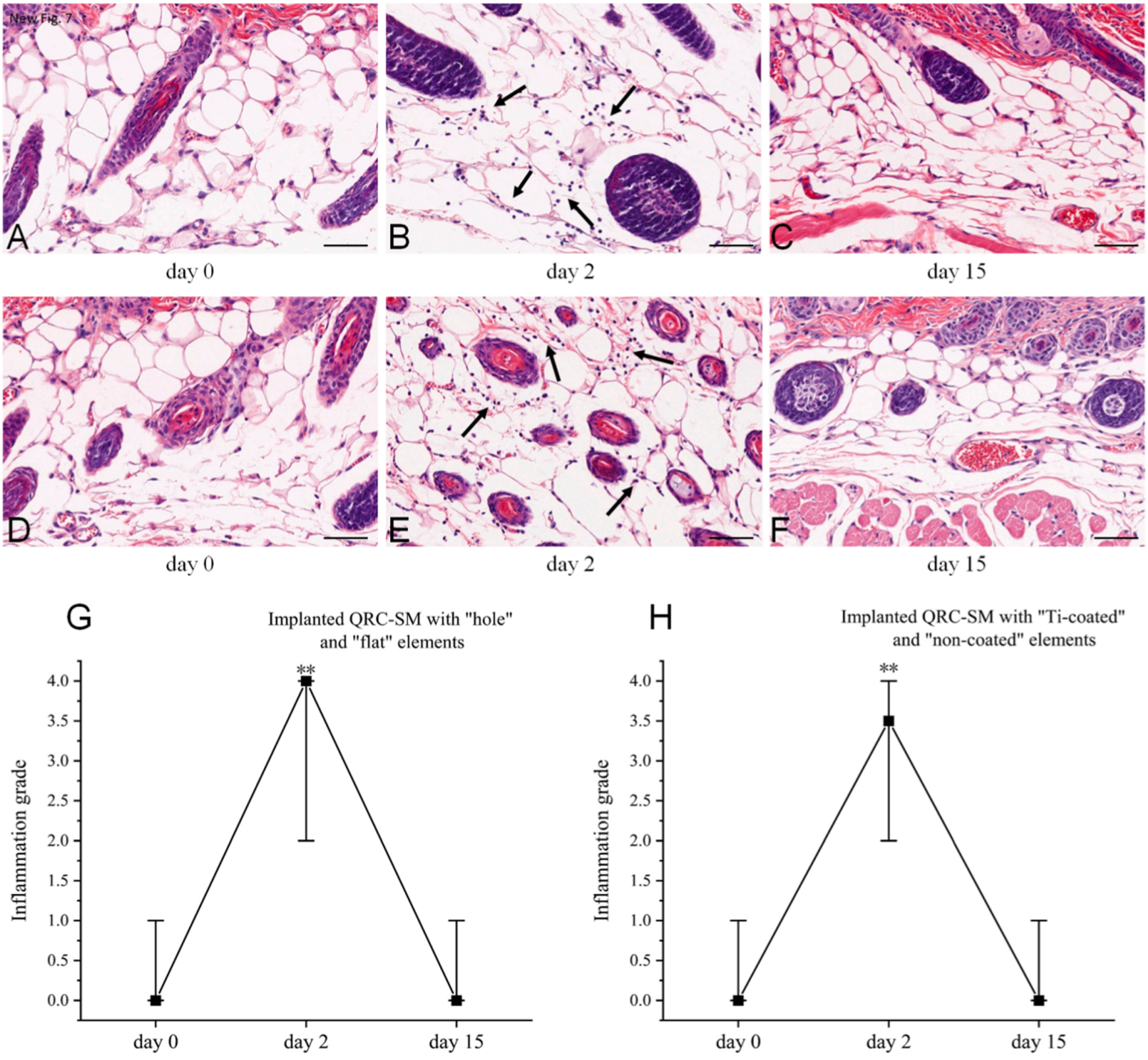

Fig. 7. Representative H&E-stained images and inflammation responses of contacting tissues (with the QRC-SM implants) after the implantation of QRC-SMs. A) to C): Representative H&E-stained images of tissue slices on day 0 (negative control), day 2, and day 15 after the implantation of QRC-SMs with "hole" and "flat" elements. D) to F): Representative H&E-stained images tissue slices on day 0 (negative control), day 2, and day 15 after the implantation of QRC-SMs with "Ti-coated" and "non-coated" elements. Black arrows: neutrophils; Scale bars, 50 μm. G) Inflammatory responses of tissue slices on day 0 (negative control), day 2, and day 15 after the implantation of QRC-SMs with "hole" and "flat" elements. H) Inflammatory response of tissue slices on day 0 (negative control), day 2, and day 15 after the implantation of QRC-SMs with "Ti-coated" and "non-coated" elements. The median ± the range is indicated at each time point. * *, $p < 0.01$ compared with day 0.

information retrieval can also be realized, and the scanning time is decreased to about 2.5 min. Although there is a tradeoff between the image resolution and the imaging speed due to the different step sizes, once the QR code pattern can be successfully recognized by the CVQR algorithm, the text information that matters can still be retrieved. Therefore, in actual applications, using a large step size to save the scanning time is desired.

2.5. Long-term stability and functionality of QRC-SM

For verifying the long-term stability and functionality of QRC-SMs, we first perform in vitro dissolution test by putting QRC-SMs with "hole" and "flat" elements and QRC-SMs with "Ti-coated" and "non-coated" elements into phosphate buffer saline (PBS) solution at 80 °C for one month, and then, these QRC-SMs are imaged by USM and AR-PAM, respectively. From the imaging results in Fig. S8 (Supporting Information), we confirm the desirable long-term stability of QRC-SMs, indicating that the information may still be retrieved after long-term implantation. In addition, in vivo multiple imaging of the same mouse during a long period of time is conducted. As shown in Fig. S9 (Supporting Information), QRC-SMs implanted in mice at 15 and 40 days after implantation surgery are imaged. The imaging for two types of QRC-SMs (with "hole" and "flat" elements; with "Ti-coated" and "non-coated" elements) are both conducted. As can be seen, the image quality remains consistent without obvious degradation throughout the monitoring period for both types of QRC-SMs. The personal information "Eric Li: Engineer of Google, 035″ and "Eric Li: Type B, Asthma" can be successfully retrieved using CVQR algorithm for all the 4 images in Fig. S9 (Supporting Information).

2.6. Long-term biosafety and biocompatibility of QRC-SM

For verifying the long-term biosafety and biocompatibility of QRC-SMs, a histology study is conducted. Histological analysis is performed on the contacting tissue at the center of the QRC-SMs implants. The representative H&E-stained images of the tissue slices on day 0 (negative control), day 2, and day 15 after implantation are shown in Fig. 7A−7F. It is obvious that inflammatory cells presented on day 2 are more than that on day 15 and day 0 (negative control). Then, the relative numbers of inflammatory cells are used to assess the inflammatory response on a 5-point ordinal severity scale: no inflammation (Grade 0), minimal (Grade 1), mild (Grade 2), moderate (Grade 3), or severe (Grade 4),[42] as shown in Fig. 7 G and 7 H. Six samples on each time point are statistically analyzed, and the two-tailed stratified Wilcoxon-Mann-Whitney test is used to calculate the p value of comparison with the tissue slices on day 0.[42] The results show that the inflammatory response on day 2 is severe, and is significantly different from that on day 0 (negative control), while the inflammatory response on day 15 is not significantly different from that on day 0 (negative control), indicating the long-term biosafety and biocompatibility of QRC-SMs after implantation.

Despite that the long-term biosafety and biocompatibility of QRC-SMs have been verified for implanted devices, a round shape is more favorable for tissue. To showcase the feasibility of fabrication of such a QRC-SM, we fabricated the QRC-SM with "hole" and "flat" elements and the QRC-SM with "Ti-coated" and "non-coated" elements with round shape by laser cutting, as shown in Fig. S10 (Supporting Information). Note that only the shape of QRC-SMs changes from square to round, while the size, material, and structure of QRC-SM elements remain unchanged. These round chips avoid sharp corners and should be even more compatible with tissue. In the future, the QRC-SMs could be potentially fabricated on flexible substrates for more conformal contact with human tissues, and both photolithography and printing can be performed on flexible substrates. With flexible substrates, the chips may also be made thinner. Caution should be paid to make sure that the flexible substrate does not deform too much to obscure the QR code pattern.

3. Discussion

In this work, QRC-SMs are designed to mimic biometrics such as fingerprints or face recognition but are inserted under the skin, so that personal information storage with high level of security can be achieved. Meanwhile, by cooperation of QRC-SM transducing systems based on optical (AR-PAM) and acoustic (USM and AR-PAM) transduction, imaging processing, and information processing, sensing individual information from body can be realized.

The main materials used in the QRC-SMs are Si, Ti, SiO_2, and PDMS, which are all biocompatible and can ensure the safety for humans. As for imaging methods, both USM and AR-PAM (non-ionizing radiation) are also considered to be safe for the human body. Si, Ti, and SiO_2 are all compatible with standard semiconductor device fabrication technologies, and thus, the QRC-SMs are highly promising for large-scale fabrication. Besides, QRC-SM patterns with a feature size of 100 μm (with elements "hole" vs. "flat") and 150 μm (with elements "Ti-coated" vs. "non-coated") allow low-cost fabrication techniques to be used, including photolithography with much relaxed requirements on resolution as we use in this work, as well as additive manufacturing techniques such as printing technology, etc.

The patterns on QRC-SMs that are hidden subcutaneously ensure the privacy of personal information, in contrast to biometrics and identity objects that are exposed (e.g., stickers, bracelets, necklaces, tattoos, and QR code identity tags). In addition, QRC-SMs almost cannot be stolen, lost, misplaced, or forgotten like physical identifying tokens, thus providing both security and convenience.

As mentioned previously, since the implantable RFID microchip has been approved by the U.S. Food and Drug Administration [20], QRC-SMs which are also implanted and used for personal identification may not suffer serious problems with bioethical implications, while more regulations and laws should be developed to further enhance the data security and privacy protection, along with the development of QRC-SMs in the future.

Compared with using RF-readers for retrieving information, we find that the cost of ultrasound and photoacoustic imaging systems is indeed much more expensive than that of RF-readers. Even so, QRC-SMs with ultrasound and photoacoustic imaging systems have wide application scenarios because of their unique advantage in security. As elaborated previously, compared with RFIDs, QRC-SMs have the advantage of more secure individual identification and authentication, because ultrasound-related imaging for QRC-SMs requires contact coupling media, which circumvents the eavesdropping and spoofing attacks by non-contact readout through wireless transmission like RFIDs. Therefore, RFIDs and QRC-SMs are complementary in the application markets. RFIDs may be used for the application scenarios with low requirements of security, such as public transportation and routine access to buildings and offices. By contrast, QRC-SMs may be used for the application scenarios with high requirements of security, such as special access to buildings (e.g., governmental agencies and armies), storing and retrieving private medical information, and banking transfer. Besides, the cost of ultrasound and photoacoustic imaging systems has a high potential to be reduced. Currently, the USM system employs a motorized stage to scan a single-element transducer. The cost of the USM system can be reduced by using a scanning mirror to replace the motorized stage [43]. Similarly, the cost of the AR-PAM system can be reduced as well, and the approach of the scanning mirror can also be applied to AR-PAM [43]. Besides, low-cost light sources using laser diodes and light-emitting diodes would further save the cost [44,45], usually at the expense of image signal-to-noise ratio (SNR). Considering that the generated photoacoustic signal amplitude of QRC-SMs is typically stronger than the intrinsic absorber in tissue (e.g., hemoglobin), it would be feasible to adopt low-cost light sources to allow enough image SNR. Moreover, towards practical applications, the state-of-the-art USM and AR-PAM

imaging systems are capable of fast and even real-time imaging, which facilitates the QR code scanning procedure [46,47]. It is worth mentioning that compared with ultrasound-related imaging, pure optical imaging is more suitable for imaging or recognition of "skin object" (in contrast to subcutaneous object) for individual identification and authentication [48].

In this work, we design the QRC-SMs based on the Version 2 with the error correction level L of QR code to demonstrate the feasibility of QRC-SMs for individual identification and authentication (https://www.qrcode.com/en/about/version.html). QRC-SMs with different Versions of QR code can be designed and fabricated to demonstrate the versatility of QRC-SMs in future applications. Once the lateral resolution of the imaging system is sufficient to resolve the adjacent elements, the QR code can be reliably recognized.

In this work, we encounter the issue of artifacts in the in vivo experiments of QRC-SMs imaged by USM in part due to mouse breathing. The methods developed to solve the issue are elaborated (see Section S1 and Fig. S11 in the Supporting Information). On the other hand, in part because the experiments of QRC-SMs imaged by AR-PAM are based on the photoacoustic signal amplitude, we do not observe obvious artifacts in AR-PAM images in the in vivo experiments.

The USM-based QRC-SM and AR-PAM-based QRC-SM have different advantages. As mentioned above, for the AR-PAM-based QRC-SM, no obvious artifacts are observed. As for USM-based QRC-SM, when the same ultrasound transducer is used for USM and AR-PAM, USM enjoys higher lateral resolution. As a result, the element length and the QRC-SM size can be made smaller, which is more friendly to human tissue for implantation. Besides, as the imaging capability of USM remains similar for different skin colors and the presence of strong optical absorbers (e.g., hair), the USM-based QRC-SM is more suitable in these cases.

One of the potential human body parts suitable for QRC-SM implantation would be the palm based on the following reasons. First, compared with the parts like the arm and thigh that are usually covered by clothes, the palm is usually exposed, which is convenient for conducting imaging (or scanning) of QRC-SMs. Secondly, there are almost no hair follicles on the palm so AR-PAM imaging of QRC-SMs under the skin of the palm would be least interfered by the hair [49]. Thirdly, the imaging capability of USM is expected to remain the same for different skin colors. As for AR-PAM, as the melanocyte density in the skin of the human palm is five times lower than that found in nonpalmoplantar sites [50], the imaging results by AR-PAM would be less influenced by the melanoma. Lastly, as QRC-SMs are designed to be implanted just under the skin (i.e., subcutaneous implantation), the ultrasound-related imaging results are not affected by the bone, which is supposed to be at a deeper location than the implanted QRC-SMs. For future applications, using a commercial high-frequency ultrasonic probe, in conjunction with ultrasound gel for ultrasound coupling, to image the human palm is a potential and convenient approach to facilitate the verification process.

We can clearly observe the trend of developing more implantable or insertable devices with technological advances [51–53]. For example, there have been various implantable medical devices such as pacemakers, cochlear implants, neurostimulation, insulin pumps, and some capsule robotics [54–56]. Such a trend also emerges for non-medical devices [57,58], such as implanted RFID microchips that are developed from a non-implanted to an implanted manner, greatly improving the convenience for applications such as entrance authentication or payment [21,22]. For implantable devices that are non-medical and go underneath the skin, they can be named insertables [57]. Different from implantable medical devices that are surgical and for restorative medical purposes, insertables are minimally invasive and aim for bringing significant convenience to human life [57,58]. In this work, the QRC-SM we propose can be categorized as "insertables", as they are designed to be placed underneath the skin and not for restorative purposes. A QRC-SM has the inherent advantage of significant convenience as an insertable. In various applications of identification and authentication, QRC-SMs are convenient as they cannot be forgotten, misplaced, and lost, so they could always be ready for medical identification, access control, and payment or banking transfer. Besides convenience, the QRC-SM can provide better privacy and security compared with biometrics or physical identification tokens based on exposed information because the personal information is hidden subcutaneously and cannot be disclosed. Comparison of the methods for individual identification and authentication is provided in Table 1. In addition, personal information that is placed underneath the skin and encoded into the QR code can enable automatic and efficient identification and authentication using machines.

4. Conclusion

In conclusion, we propose and demonstrate that implantable and minimally-invasive QRC-SMs can be an effective approach to carry useful and private information, and the information can be retrieved by imaging techniques and open-source QR code recognition algorithm, thus enabling various applications in individual identification and authentication. Two schemes, QRC-SMs with "hole" and "flat" elements imaged by USM and QRC-SMs with "Ti-coated" and "non-coated" elements imaged by AR-PAM have been designed and implemented. In *ex vivo* and in vivo experiments, QRC-SMs, together with the corresponding imaging systems and the QR code recognition algorithm, have realized personal information storage, QR code image acquisition, and QR code information retrieval, demonstrating the feasibility of QRC-SMs for individual identification and authentication. Combining the advantages of high convenience, privacy, security, and automatic information retrieval, QRC-SM technique is promising and has the potential to be one of the next-generation identification and authentication technologies in the future.

5. Material and methods

5.1. Imaging systems

QRC-SMs with "hole" and "flat" elements are imaged by USM. A focused ultrasound transducer is used to emit acoustic waves and then receive the backscattered acoustic waves. The focused transducer is made by attaching an acoustic lens (45006, Edmund Optics, NJ) to a 50-MHz flat ultrasonic transducer (V214-BC-RM, 77% bandwidth, Panametrics NDT, MA), which provides an NA of 0.44 and a focal length of 6.7 mm. A pulse receiver (5073PR, Olympus Inc.) is utilized to drive the focused transducer for generating ultrasound waves, and the pulse repetition frequency is set as 200 Hz. During image acquisition, the focused transducer is fixed with a 2D motorized stage (M-L01.2A1, Physik Instrumente) for 2D raster scanning. Backscattered ultrasound signals are recorded by a digitizer (CSE1422, Gage) and then stored in a

Table 1
Comparison of the methods for individual identification and authentication.

Methods	Security and privacy	Convenience	Refs.
Account and password	Middle	Middle	[9,10]
Biometrics[a]	Low	High	[12,13]
Exposed identity object[b]	Low	Middle	-
RFID-based object (non-implant)[c]	Middle	Middle	[16]
RFID implant	Middle	High[d]	[21,23]
QRC-SM	High	High[d]	This work

[a] Face, iris, fingerprint, voice, etc.
[b] Sticker, bracelet, necklace, tattoo, and QR code identity tag (tape, sticker, tattoo, etc.).
[c] RFID-based card, bracelet, necklace, etc.
[d] After implantation.

computer. Especially for imaging QRC-SMs covered by 2.3-mm-layer chicken breast tissue and imaging QRC-SMs implanted underneath mouse skin in *ex vivo* and in vivo experiments, respectively, the pulse receiver also serves as a preamplifier to amplify the received ultrasound signals with gain of 20 dB and 6 dB, respectively.

QRC-SMs with "Ti-coated" and "non-coated" elements are imaged by AR-PAM. A 6 ns pulsed laser (Spitlight DPSS EVO I, InnoLas, German) with pulse repetition frequency of 100 Hz and wavelength of 1064 nm (and 670 nm) is used for photoacoustic excitation. The laser is coupled into a multimode optical patch cord (MHP910L02, Thorlabs). The same focused transducer (used in USM mentioned above) is used to receive photoacoustic waves. During image acquisition, the imaging head of AR-PAM, consisting of the laser illumination parts and the acoustic detection parts, is fixed with the same 2D motorized stage for raster scanning. Detected photoacoustic signals are amplified by a low-noise preamplifier (ZFL-500LN+, Mini-Circuits), recorded by a digitizer (CSE1422, Gage), and then stored in a computer. For imaging bare QRC-SMs, the laser fluence is measured as 0.18 mJ/cm^2. For *ex vivo* and in vivo experiments, the laser fluence is measured as 12.27 mJ/cm^2 and 1.47 mJ/cm^2, respectively. All the values are lower than American National Standards Institute safety limit (100 mJ/cm^2 for 1064 nm wavelength). In addition, besides 1064 nm wavelength, laser at 670 nm wavelength is also used for in vivo experiment, and the laser fluence is measured as 3.93 mJ/cm^2, which is also lower than American National Standards Institute safety limit (about 20 mJ/cm^2 for the 670 nm wavelength).

For lateral resolution measurements of USM and AR-PAM, the one-dimensional (1D) profiles of a sharp edge coated with chromium (on the top surface; for optical absorption) are imaged by USM and AR-PAM, respectively. The 1D profiles are fitted by edge spread function (ESF). Line-spread function (LSF) is then obtained by taking the first derivative of the ESF, and the lateral resolution can be estimated by the full width at half maximum of the LSF.

5.2. Nude mouse preparation for in vivo experiments

Two 8-weeks-old Balb/c nude mice are used for the results in Figs. 4 and 6. One is for implanting a QRC-SM with "hole" and "flat" elements, and the other is for implanting a QRC-SM with "Ti-coated" and "non-coated" elements. During implantation, the mice are anesthetized by the isoflurane anesthesia machine (R500IP, RWD Life Science) with a gas mixture of 1% isoflurane and oxygen. For the mouse to be implanted with the QRC-SM with "hole" and "flat" elements, a 4.5 mm incision is made at the lower part of the dorsal for implantation, while for the mouse to be implanted with the QRC-SM with "Ti-coated" and "non-coated" elements, the incision is about 6.5 mm. After incision, the skin near the incision is lifted using a tweezer, and then the QRC-SM is implanted underneath the skin. After implantation, the small incision is closed. During imaging, the mouse is also anesthetized and is fixed using a homemade fixation device to avoid potential motion artifacts. All experimental animal procedures are carried out in conformity with the laboratory animal protocol approved by Laboratory Animal Care Committee at Shanghai Jiao Tong University.

5.3. Image processing

For QRC-SMs with "hole" and "flat" elements, the time at the peak of the envelope of ultrasound A-line signals is used to generate the 2D depth-encoded image. Then, the depth-encoded image is fed into the CVQR algorithm to retrieve personal information. For QRC-SMs with "Ti-coated" and "non-coated" elements, the photoacoustic A-line signals are recorded, and MAP along the axial direction is applied to the 3D data to obtain the 2D MAP image. Similarly, the MAP image is then fed into CVQR algorithm to retrieve personal information. Directly inputting depth-encoded images or MAP images into CVQR algorithm enables *automatic and efficient* identification and authentication.

The presented depth-encoded images and MAP images in this paper are output by MATLAB software. When using WeChat application to test the information retrieval, the colormap choice, the display effect of the computer screen, the light shooting angle, and the camera performance would all affect the retrieval result, which is a little different from directly inputting the depth-encoded images or MAP images into the CVQR algorithm for information retrieval. We have performed a test using WeChat application (version 14.0.1) on iPhone XR, which can successfully retrieve information from all the depth-encoded images and MAP images presented in this manuscript. For an Android smartphone, WeChat application (version 8.0.16) on Mi Mix2 (manufactured by Xiaomi) can also realize information retrieval.

CRediT authorship contribution statement

Conceptualization: S.C., R.Y. and N.W. Methodology: S.C., R.Y., N. W., P.Z., Z.L., W.N., and X.R. Investigation: N.W., P.Z., Z.L., Z.L., W.N., X.R., S.W. S.L. and J.Z. Visualization: N.W., P.Z., Z.L. and P.H. Supervision: S.C. and R.Y. Writing—original draft: N.W. and P.Z. Writing—review & editing: S.C., R.Y. and M.S.

Declaration of Competing Interest

The authors declare that they have no known competing financial interests or personal relationships that could have appeared to influence the work reported in this paper.

Data Availability

Data will be made available on request.

Acknowledgments

N. W and P. Z contributed equally to this work. The authors acknowledge the support from National Natural Science Foundation of China (NSFC) (grants 62235013, 82130057, 61775134, 62104140 and U21A20505), Science and Technology Commission of Shanghai Municipality (STCSM) Natural Science Project General Program (grants 22ZR1428900 and 21ZR1433800), and Shanghai Sailing Program (grant 19YF1424900). The authors acknowledge the Center for Advanced Electronic Materials and Devices (AEMD) of Shanghai Jiao Tong University for the support in device fabrication.

Appendix A. Supporting information

Supplementary data associated with this article can be found in the online version at doi:10.1016/j.pacs.2023.100504.

References

[1] R.S. Sandhu, P. Samarati, Access control: Principle and practice, IEEE Commun. Mag. 32 (1994) 40–48, https://doi.org/10.1109/35.312842.
[2] G. Horn, B. Preneel, Authentication and payment in future Mobile Systems, J. Comput. Secur. 8 (2000) 183–207, https://doi.org/10.3233/jcs-2000-82-306.
[3] T. Alladi, S. Chakravarty, V. Chamola, M. Guizani, A lightweight authentication and attestation scheme for in-transit vehicles in iov scenario, IEEE Trans. Veh. Technol. 69 (2020) 14188–14197, https://doi.org/10.1109/tvt.2020.3038834.
[4] M.K. Khan, S. Kumari, An authentication scheme for secure access to healthcare services, J. Med. Syst. (2013) 37, https://doi.org/10.1007/s10916-013-9954-3.
[5] R.I. García Betances, M.K. Huerta, A review of automatic patient identification options for public health care centers with restricted budgets, Online J. Public Health Inform. (2012) 4, https://doi.org/10.5210/ojphi.v4i1.4011.
[6] F.W. Newell, Patient identification and patient confidentiality, Am. J. Ophthalmol. 81 (1976) 363–364, https://doi.org/10.1016/0002-9394(76)90256-7.
[7] J.D. Williams, J.A. Xenakis, A.B. JD, Establishing identity during a disaster: The Emergency Management Assistance Compact and the first responder authentication credential, J. Emerg. Manag. 6 (2008) 11, https://doi.org/10.5055/jem.2008.0041.
[8] M. Zviran, Z. Erlich, Identification and authentication: Technology and implementation issues, Commun. Assoc. Inf. Syst. (2006) 17, https://doi.org/10.17705/1cais.01704.

[9] A.K. Jain, K. Nandakumar, Biometric authentication: System security and user privacy, Computer 45 (2012) 87–92, https://doi.org/10.1109/mc.2012.364.

[10] M.S. Gerashchenko, A.G. Fateev, M.V. Markuleva, A.N. Astafyev, S.L. Zefirov, S. I. Gerashchenko, Biometric identification and authentication based on a new method of a pulse wave contour forming, J. Phys. Conf. Ser. 1679 (2020), 022017, https://doi.org/10.1088/1742-6596/1679/2/022017.

[11] W. Meng, D.S. Wong, S. Furnell, J. Zhou, Surveying the development of biometric user authentication on mobile phones, IEEE Commun. Surv. Tutor. 17 (2015) 1268–1293, https://doi.org/10.1109/comst.2014.2386915.

[12] Z. Rui, Z. Yan, A survey on biometric authentication: Toward secure and privacy-preserving identification, IEEE Access 7 (2019) 5994–6009, https://doi.org/10.1109/access.2018.2889996.

[13] E. Pagnin, A. Mitrokotsa, Privacy-preserving biometric authentication: Challenges and directions, Secur. Commun. Netw. 2017 (2017) 1–9, https://doi.org/10.1155/2017/7129505.

[14] C.-T. Yen, M.-H. Guo, N.-W. Lo, D.-J. Deng, Authentication with low-cost RFID tags in Mobile Networks, Secur. Commun. Netw. 6 (2013) 1021–1027, https://doi.org/10.1002/sec.667.

[15] M.M. Aung, Y.S. Chang, J.-U. Won, Emerging RFID/USN applications and challenges, Int. J. RFID Secur. Cryptogr. 1 (2012) 3–8, https://doi.org/10.20533/ijrfidsc.2046.3715.2012.0001.

[16] P. Rotter, B. Daskala, R. Compano, RFID implants: Opportunities and and challenges for identifying people, IEEE Technol. Soc. Mag. 27 (2008) 24–32, https://doi.org/10.1109/mts.2008.924862.

[17] T. Kriplean, E. Welbourne, N. Khoussainova, V. Rastogi, M. Balazinska, G. Borriello, T. Kohno, D. Suciu, Physical access control for captured RFID data, IEEE Pervasive Comput. 6 (2007) 48–55, https://doi.org/10.1109/mprv.2007.81.

[18] P. Verma, A. Kumar, S. Chachada, Enhancing security of contactless payment using RFID and GSM, Int. J. Comput. Appl. Technol. Res. 7 (2018) 422–424, https://doi.org/10.7753/ijcatr0712.1004.

[19] A. Abugabah, N. Nizamuddin, A. Abuqabbeh, A review of challenges and barriers implementing RFID technology in the Healthcare Sector, Procedia Comput. Sci. 170 (2020) 1003–1010, https://doi.org/10.1016/j.procs.2020.03.094.

[20] B. Werber, A. Žnidaršič, The use of subcutaneous RFID microchip in health care - A willingness to challenge, Health Technol. 5 (2015) 57–65, https://doi.org/10.1007/s12553-015-0105-3.

[21] J. Halamka, A. Juels, A. Stubblefield, J. Westhues, The security implications of Verichip Cloning, J. Am. Med. Inform. Assoc. 13 (2006) 601–607, https://doi.org/10.1197/jamia.m2143.

[22] A. Masters, K. Michael, Lend me your arms: The use and implications of humancentric RFID, Electron. Commer. Res. Appl. 6 (2007) 29–39, https://doi.org/10.1016/j.elerap.2006.04.008.

[23] S.R. Moosavi, A. Hakkala, J. Isoaho, S. Virtanen, J. Isoaho, Specification analysis for secure RFID implant systems, Int. J. Comput. Theory Eng. 6 (2014) 177–188, https://doi.org/10.7763/ijcte.2014.v6.858.

[24] A. Mishra, M. Mathuria, A review on QR code, Int. J. Comput. Appl. 164 (2017) 17–19, https://doi.org/10.5120/ijca2017913739.

[25] S. Elhajji, G. Orhanou, Y. Kouraogo, Advanced security of two factor-authentication system using stego QR-code, Int. J. Inf. Comput. Secur. 12 (2020) 1, https://doi.org/10.1504/ijics.2020.10020446.

[26] K.-C. Liao, W.-H. Lee, A novel user authentication scheme based on QR-code, J. Netw. (2010) 5, https://doi.org/10.4304/jnw.5.8.937-941.

[27] P.-C. Huang, C.-C. Chang, Y.-H. Li, Y. Liu, Efficient access control system based on aesthetic QR code, Pers. Ubiquitous Comput. 22 (2017) 81–91, https://doi.org/10.1007/s00779-017-1089-y.

[28] R. Focardi, F.L. Luccio, H.A.M. Wahsheh, Usable security for QR code, J. Inf. Secur. Appl. 48 (2019), 102369, https://doi.org/10.1016/j.jisa.2019.102369.

[29] V. Uzun, S. Bilgin, Evaluation and implementation of QR code identity tag system for healthcare in Turkey, SpringerPlus (2016) 5, https://doi.org/10.1186/s40064-016-3020-9.

[30] O. Ogunlade, J.O.Y. Ho, T.L. Kalber, R.E. Hynds, E. Zhang, S.M. Janes, M. A. Birchall, C.R. Butler, P. Beard, Monitoring neovascularization and integration of decellularized human scaffolds using photoacoustic imaging, Photoacoustics 13 (2019) 76–84, https://doi.org/10.1016/j.pacs.2019.01.001.

[31] P.C. Lin, Optical imaging and tumor angiogenesis, J. Cell. Biochem. 90 (2003) 484–491, https://doi.org/10.1002/jcb.10630.

[32] V. Periyasamy, N. Das, A. Sharma, M. Pramanik, 1064 nm acoustic resolution photoacoustic microscopy, J. Biophoton. (2019) 12, https://doi.org/10.1002/jbio.201800357.

[33] K. Sivasubramanian, V. Periyasamy, R.A. Dienzo, M. Pramanik, Hand-held, clinical dual mode ultrasound - photoacoustic imaging of rat urinary bladder and its applications, J. Biophoton. (2018) 11, https://doi.org/10.1002/jbio.201700317.

[34] A.J. Festas, A. Ramos, J.P. Davim, Medical devices biomaterials – a review, Proc. Inst. Mech. Eng. Part L J. Mater. Des. Appl. 234 (2019) 218–228, https://doi.org/10.1177/1464420719882458.

[35] W.S. Werner, K. Glantschnig, C. Ambrosch-Draxl, Optical constants and inelastic electron-scattering data for 17 elemental metals, J. Phys. Chem. Ref. Data 38 (2009) 1013–1092, https://doi.org/10.1063/1.3243762.

[36] Rodríguez-de Marcos, L.V., Larruquert, J.I., Méndez, J.A., Aznárez, J.A, Self-consistent optical constants of SiO_2 and Ta_2O_5 films, Opt. Mater. Express 6 (2016) 3622, https://doi.org/10.1364/ome.6.003622.

[37] I. Miranda, A. Souza, P. Sousa, J. Ribeiro, E.M. Castanheira, R. Lima, G. Minas, Properties and applications of PDMS for biomedical engineering: a review, J. Funct. Biomater. 13 (2021) 2, https://doi.org/10.3390/jfb13010002.

[38] Opencv, 2021. Opencv_contrib/modules/wechat_qrcode/SRC at master·opencv/opencv_contrib [WWW Document]. GitHub. URL https://github.com/opencv/opencv_contrib/tree/master/modules/wechat_qrcode/src (accessed 11.24.22).

[39] C.-W. Wei, T.-M. Nguyen, J. Xia, B. Arnal, E.Y. Wong, I.M. Pelivanov, M. O'Donnell, Real-time integrated photoacoustic and ultrasound (PAUS) imaging system to guide interventional procedures: Ex vivo study, IEEE Trans. Ultrason. Ferroelectr. Freq. Control 62 (2015) 319–328, https://doi.org/10.1109/tuffc.2014.006728.

[40] M. Moothanchery, K. Dev, G. Balasundaram, R. Bi, M. Olivo, Acoustic resolution photoacoustic microscopy based on microelectromechanical systems scanner, J. Biophoton. 13 (2019), https://doi.org/10.1002/jbio.201960127.

[41] J. Yao, L.V. Wang, Photoacoustic microscopy, Laser Photonics Rev. 7 (2013) 758–778, https://doi.org/10.1002/lpor.201200060.

[42] A. Dalu, B.S. Blaydes, L.G. Lomax, K.B. Delclos, A comparison of the inflammatory response to a polydimethylsiloxane implant in male and female Balb/C Mice, Biomaterials 21 (2000) 1947–1957, https://doi.org/10.1016/s0142-9612(00)00078-8.

[43] D.C. De Cai, Z.L. Zhongfei Li, S.-L.C. Sung-Liang Chen, Photoacoustic microscopy by scanning mirror-based synthetic aperture focusing technique, Chin. Opt. Lett. 13 (2015) 101101–101104, https://doi.org/10.3788/col201513.101101.

[44] H. Zhong, T. Duan, H. Lan, M. Zhou, F. Gao, Review of low-cost photoacoustic sensing and imaging based on laser diode and light-emitting diode, Sensors 18 (2018) 2264, https://doi.org/10.3390/s18072264.

[45] M. Erfanzadeh, Q. Zhu, Photoacoustic imaging with low-cost sources; a review, Photoacoustics 14 (2019) 1–11, https://doi.org/10.1016/j.pacs.2019.01.004.

[46] J.W. Baik, J.Y. Kim, S. Cho, S. Choi, J. Kim, C. Kim, Super wide-field photoacoustic microscopy of animals and humans in vivo, IEEE Trans. Med. Imaging 39 (2020) 975–984, https://doi.org/10.1109/tmi.2019.2938518.

[47] J. Kim, J.Y. Kim, S. Jeon, J.W. BAIK, S.H. Cho, C. Kim, Super-resolution localization photoacoustic microscopy using intrinsic red blood cells as contrast absorbers, Light. Sci. Appl. 8 (2019), https://doi.org/10.1038/s41377-019-0220-4.

[48] Q. Zhao, H. Li, Z. Yu, C.M. Woo, T. Zhong, S. Cheng, Y. Zheng, H. Liu, J. Tian, P. Lai, Speckle-based optical cryptosystem and its application for human face recognition via deep learning, Adv. Sci. 9 (2022) 2202047, https://doi.org/10.1002/advs.202202407.

[49] G. Szabo, The regional anatomy of the human integument with special reference to the distribution of hair follicles, sweat glands and melanocytes, Philos. Trans. R. Soc. B 252 (1967) 447–485, https://doi.org/10.1098/rstb.1967.0029.

[50] Y. Yamaguchi, S. Itami, H. Watabe, K. Yasumoto, Z.A. Abdel-Malek, T. Kubo, F. Rouzaud, A. Tanemura, K. Yoshikawa, V.J. Hearing, Mesenchymal-epithelial interactions in the skin: increased expression of dickkopf1 by palmoplantar fibroblasts inhibits melanocyte growth and differentiation, J. Cell Biol. 165 (2004) 275–285, https://doi.org/10.1083/jcb.200311122.

[51] Y. Song, J. Min, W. Gao, Wearable and implantable electronics: Moving toward precision therapy, ACS Nano 13 (2019) 12280–12286, https://doi.org/10.1021/acsnano.9b08323.

[52] W.B. Han, G.-J. Ko, T.-M. Jang, S.-W. Hwang, Materials, devices, and applications for wearable and implantable electronics, ACS Appl. Electron. Mater. 3 (2021) 485–503, https://doi.org/10.1021/acsaelm.0c00724.

[53] J. Li, R. Li, H. Du, Y. Zhong, Y. Chen, K. Nan, S.M. Won, J. Zhang, Y. Huang, J. A. Rogers, Ultrathin, transferred layers of metal silicide as Faradaic electrical interfaces and biofluid barriers for flexible Bioelectronic implants, ACS Nano 13 (2019) 660–670, https://doi.org/10.1021/acsnano.8b07806.

[54] Y.S. Choi, R.T. Yin, A. Pfenniger, J. Koo, R. Avila, K. Benjamin Lee, S.W. Chen, G. Lee, G. Li, Y. Qiao, A. Murillo-Berlioz, A. Kiss, S. Han, S.M. Lee, C. Li, Z. Xie, Y.-Y. Chen, A. Burrell, B. Geist, H. Jeong, J. Kim, H.-J. Yoon, A. Banks, S.-K. Kang, Z. J. Zhang, C.R. Haney, A.V. Sahakian, D. Johnson, T. Efimova, Y. Huang, G. D. Trachiotis, B.P. Knight, R.K. Arora, I.R. Efimov, J.A. Rogers, Fully implantable and bioresorbable cardiac pacemakers without leads or batteries, Nat. Biotechnol. 39 (2021) 1228–1238, https://doi.org/10.1038/s41587-021-00948-x.

[55] S.M. Won, E. Song, J.T. Reeder, J.A. Rogers, Emerging modalities and implantable technologies for neuromodulation, Cell 181 (2020) 115–135, https://doi.org/10.1016/j.cell.2020.02.054.

[56] J. Min, Y. Yang, Z. Wu, W. Gao, Robotics in the gut, Adv. Ther. 3 (2019) 1900125, https://doi.org/10.1002/adtp.201900125.

[57] K.J. Heffernan, F. Vetere, S. Chang, Insertables, Interactions 23 (2015) 52–56, https://doi.org/10.1145/2843588.

[58] K.J. Heffernan, F. Vetere, S. Chang, Towards insertables: Devices inside the human body, First Monday (2017) 22, https://doi.org/10.5210/fm.v22i3.6214.

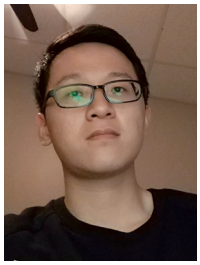

Nan Wan received his B.S. degree and M.S. degree in the major of Precision Instrument from Chongqing University in 2016 and 2019, respectively. Also, he joined the Micro Analysis Systems Laboratory at the University of Tennessee, Knoxville for biochemical molecules detection research in 2018. He then joined the University of Michigan-Shanghai Jiao Tong University Joint Institute in 2019 as a graduate student. His research interest is developing photoacoustic imaging systems for multiple applications.

Pengcheng Zhang received a B.S. degree in electrical engineering from Sichuan University, Chengdu, Sichuan, China. He is currently a Ph.D. candidate at the University of Michigan-Shanghai Jiao Tong University Joint Institute, Shanghai Jiao Tong University, Shanghai, China. His research interests include signal transduction, damping mechanisms and application of nanoelectromechanical systems (NEMS) based on 2D materials.

Zuheng Liu received the B.S. degree in electrical and computer engineering from Shanghai Jiao Tong University, Shanghai, China, and now pursuing his Ph.D. at electrical science and engineering at Shanghai Jiao Tong University, China. His research interests include nano electrical and mechanical system (NEMS), bio-implanted electronic devices, and the design and applications of NEMS/MEMS sensors.

Zhe Li received the MD. and Ph.D. degree in Emergency medicine Shanghai Jiaotong University School of Medicine, an intensivist from Department of Critical Care Medicine, Ren Ji Hospital, Shanghai, with a subspecialty interest in the management of sepsis induced endothelial injury , acute respiratory failure and the clinical application of EIT.

Niu Wei received the Master of Internal Medicine from School of Medicine, Shanghai Jiao Tong University, Shanghai, China. She is working in Huadong Hospital, Fudan University, Shanghai now. Her main research interest is peritoneal dialysis, especially peritoneal fibrosis caused by peritoneal dialysis.

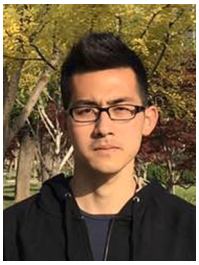

Xiuye Rui received the bachelor's degree in automation and master's degree in control engineering from Tianjin University of Technology. Then he got two work experiences in the past four years, worked with Hikvision as an algorithm engineer for the first three years, and was responsible for Providing algorithm library for security products. Next, he worked with Lotus Technology as a Senior Engineer of Intelligent Driving Algorithm Development for one year, involved in the algorithm development of the prediction module and the risk module. Now, he is working at Bosch Future Intelligent Driving and Control (Shanghai) R&D Center.

Shibo Wang received the Bachelor degree in Electrical and Computer Engineering from the Shanghai Jiao Tong University, Shanghai, China. He's currently studying in Case Western Reserve University for master's degree in Computer Engineering. His research interests include Computer Vision and Deep Learning.

Myeongsu Seong received the Ph.D. degree in biomedical science and engineering from the Gwangju Institute of Science and Technology, Gwangju, Republic of Korea, and postdoctoral training at the Shanghai Jiao Tong University, China. He is currently an Assistant Professor at Department of Mechatronics and Robotics, School of Advanced Technology, Xi'an Jiaotong–Liverpool University China. His research interests include the development and applications of diffuse optical spectroscopy/imaging, diffuse correlation spectroscopy, diffuse speckle contrast flowmetry, and photoacoustic imaging technology.

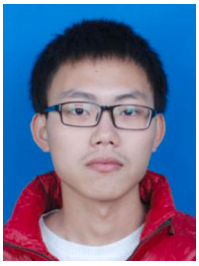

Pengbo He received the B.S. degree in Electrical and Computer Engineering from University of Michigan-Shanghai Jiao Tong University Joint Institute. His research interest is developing applications for photoacoustic microscopy.

Siqi Liang received the B.S. degree in Optoelectronic Information of Science and Engineering from Northwestern Polytechnical University. In 2018, he joined the University of Michigan-Shanghai Jiao Tong University Joint Institute, Shanghai Jiao Tong University, Shanghai, China, to continue further studies. His research interest is image processing in photoacoustic imaging.

Jiasheng Zhou received his B.S. degree in Electronic Science and Technology from Shandong University and the M.S. degree in Optics from East China Normal University. In 2018, he joined the University of Michigan-Shanghai Jiao Tong University Joint Institute, Shanghai Jiao Tong University, Shanghai, China, as a graduate student. His research interests include fast scanning photoacoustic imaging and non-contact photoacoustic imaging.

Rui Yang received the Ph.D. degree in electrical engineering from Case Western Reserve University, Ohio, USA in 2016, and post-doctoral training at Stanford University, USA. He is currently an Associate Professor at the University of Michigan-Shanghai Jiao Tong University Joint Institute, Shanghai Jiao Tong University, Shanghai, China. His research interests include nanoelectromechanical systems (NEMS) based on 2D Materials, in-memory computing and neuromorphic computing using nonvolatile memories, and optoelectronic devices based on emerging materials. He was a recipient of the Shanghai "Rising Star" Program and Shanghai Sailing Program.

Sung-Liang Chen received the Ph.D. degree in electrical engineering from the University of Michigan, Ann Arbor, MI, USA, and post-doctoral training at the University of Michigan Medical School, USA. He is currently an Associate Professor at the University of Michigan-Shanghai Jiao Tong University Joint Institute, Shanghai Jiao Tong University, Shanghai, China. His research interests include photoacoustic imaging technology and applications, optical imaging systems, and miniature photoacoustic transducers and ultrasound sensors. He was a recipient of the Shanghai Pujiang Talent Award.